Single Si-V^- Centers in Low-Strain Nanodiamonds with Bulklike Spectral Properties and Nanomanipulation Capabilities

Lachlan J. Rogers,[1,2] Ou Wang,[3,4] Yan Liu,[3] Lukas Antoniuk,[3] Christian Osterkamp,[3,4,5] Valery A. Davydov,[6] Viatcheslav N. Agafonov,[7] Andrea B. Filipovski,[3] Fedor Jelezko,[3,4] and Alexander Kubanek[3,4,*]

[1] *Department of Physics and Astronomy, Macquarie University, Sydney, New South Wales 2109, Australia*
[2] *ARC Centre of Excellence for Engineered Quantum Systems, Sydney, New South Wales 2109, Australia*
[3] *Institute for Quantum Optics,University Ulm, Albert-Einstein-Allee 11, 89081 Ulm, Germany*
[4] *Center for Integrated Quantum Science and Technology, University of Ulm, Albert-Einstein-Allee 11, 89081 Ulm, Germany*
[5] *Institute of Electron Devices and Circuits, University of Ulm, Albert-Einstein-Allee 45, 89081 Ulm, Germany*
[6] *L.F. Vereshchagin Institute for High Pressure Physics, Russian Academy of Sciences, Troitsk, Kaluzhskoe shosse 14, Moscow 142190, Russia*
[7] *GREMAN, UMR CNRS CEA 6157, Université F. Rabelais, Parc de Grandmont, 37200 Tours, France*

(Received 20 April 2018; revised manuscript received 20 November 2018; published 28 February 2019)

We report on the isolation of single negatively-charged-silicon-vacancy (Si-V^-) centers in nanodiamonds. We observe the fine structure of single Si-V^- centers with reduced inhomogeneous ensemble linewidth below the excited-state splitting, stable optical transitions, good polarization contrast, and excellent spectral stability under resonant excitation. On the basis of our experimental results, we develop an analytical strain model where we extract the ratio between strain coefficients of excited and ground states as well the intrinsic zero-strain spin-orbit splittings. The observed strain values are as low as the best values in low-strain bulk diamond. We achieve our results by means of H-plasma treatment of the diamond surface and in combination with resonant and off-resonant excitation. Our work paves the way for indistinguishable, single-photon emission. Furthermore, we demonstrate controlled nanomanipulation by an atomic-force-microscope cantilever of one- and two-dimensional alignments with an accuracy of about 10 nm, as well as new tools including dipole rotation and cluster decomposition. Combined, our results show the potential to utilize Si-V^- centers in nanodiamonds for controlled interfacing via optical coupling of individually-well-isolated atoms for bottom-up assemblies of complex quantum systems.

DOI: 10.1103/PhysRevApplied.11.024073

I. INTRODUCTION

Experimental quantum optics has gradually shifted focus from testing fundamentals of quantum mechanics using isolated quantum systems such as atoms or photons [1,2] toward the development of quantum technologies using many connected quantum systems. Applications include quantum computation (ion traps and superconducting technology have achieved several quantum bits [3,4]) and low-entropy systems, realized in atom-by-atom assemblies of up to 100 atoms in one-dimensional defect-free arrays [5]. The central challenge is to balance the need for quantum systems to be well isolated from their environment with the competing requirement that they interact with each other via well-controlled coupling. Coupling mechanisms include magnetic interaction, dipole-dipole interaction, and long-range interaction between distant atoms mediated by photons as used in photonic quantum technologies [6] or distributed quantum networks [7,8]. Efficient interfacing requires precise positioning on the relevant scale of the specific coupling mechanism, which is smaller than the electromagnetic field wavelength for optical coupling.

Semiconductor quantum optics is particularly well suited for constructing scalable devices satisfying this requirement, and the negatively-charged-silicon-vacancy (Si-V^-) color center in diamond has emerged as an excellent optical-spin candidate. Single Si-V^- centers have been coupled to all-diamond photonic platforms [9,10] and are good sources of indistinguishable photons [11,12] with lifetime-limited spectral linewidth, low spectral diffusion in low-strain diamond hosts [13], and a high Debye-Waller factor [14]. Arrays of bright Si-V^- centers have been created by ion implantation with a yield of up to 15%

*alexander.kubanek@uni-ulm.de

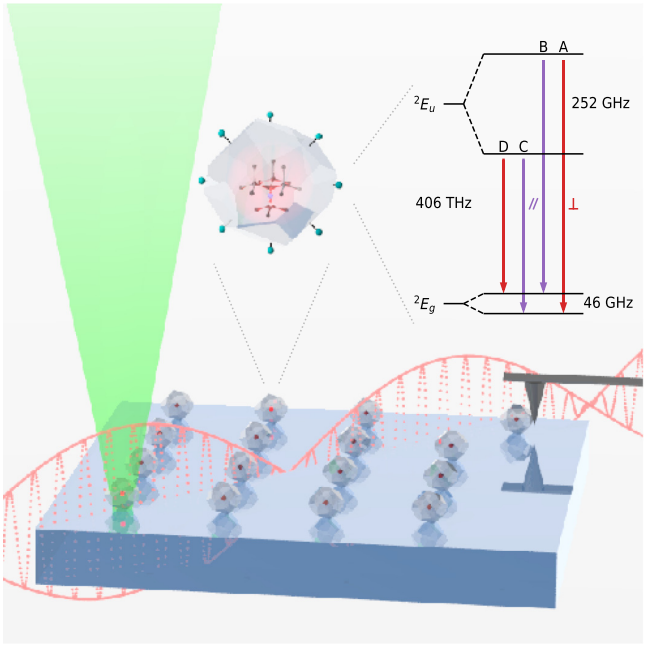

FIG. 1. A conceptual design for single-emitter assemblies involves bottom-up formation from preselected nanodiamonds. Hydrogen surface termination is found to improve the optical properties of Si-V^- centers in nanodiamonds, which could enable deterministic creation of emitter arrays for quantum applications. The optical properties of the Si-V^- center in diamond arise from four optical transitions between doublet ground and excited states.

[15]. However a bottom-up approach using single Si-V^- centers in preselected nanodiamonds (NDs) could make possible deterministic emitter assemblies where hardware errors could be corrected by replacement of defective NDs (Fig. 1). This offers a wide-ranging flexibility for hybrid photonic platforms [16–18]. Despite progress with Si-V^- centers in NDs demonstrating nearly-lifetime-limited linewidth [19], they still suffer from surface effects and from a highly strained diamond host with broad inhomogeneous linewidth and large spectral instability and, furthermore, no deterministic way to obtain single NDs containing single Si-V^- centers.

Here we show that Si-V^- centers contained in NDs have improved optical properties after surface treatment in hydrogen plasma, and demonstrate that ND Si-V^- centers are capable of providing atomlike spectral properties as in bulk diamond. Single Si-V^- centers are isolated in NDs and their optical transition fine structure is used to explore the strain of their host crystal environments, with 70% of the Si-V^- centers exhibiting transverse-strain splitting similar to the lowest-strain bulk diamond. The natural distribution of strain in the NDs provides the first systematic inference of the Si-V^- zero-strain orbital splitting, and also the ratio of transverse-strain splitting coefficients between ground and excited states. Low-strain Si-V^- centers in NDs are shown to exhibit a high degree of optical polarization contrast, almost-Fourier-limited linewidth, and spectral stability within the Fourier-limited linewidth over 10 min. In addition, we demonstrate nanomanipulation abilities necessary to construct arrays of Si-V^- emitters for hybrid photonic platforms. An atomic-force-microscope (AFM) probe is used to position NDs in one- and two-dimensional arrays with an accuracy below the uncertainties of the emitter localization of typically approximately 25 nm limited by the extend of the ND and the lateral resolution of the AFM. This technique is also shown to be capable of rotating NDs for dipole alignment, and decomposing ND clusters. These abilities to control and nanomanipulate single Si-V^- centers in NDs with sizes of a few tens of nanometers and large spectral homogeneity expand a toolbox already consisting of pick-and-place techniques [16,18,20]. Our results open new possibilities to optically couple arrays of Si-V^- centers in NDs, exploring novel routes for hybrid quantum technology in fields such as quantum networks, quantum sensing, and quantum simulations.

II. METHODS

A. High-pressure high-temperature synthesis of NDs

The Si-doped NDs are synthesized following the receipe in Ref. [21]. High pressure high-temperature (HPHT) synthesis of luminescent NDs is performed on the basis of a fluorohydrocarbon growth system without metal catalysts [21]. Naphthalene ($C_{10}H_8$; Chemapol) and highly fluorinated graphite $CF_{1.1}$ (Aldrich Chemical) with impurity content less than 0.5% are used as initial hydrocarbon and fluorocarbon components of the growth system. Tetrakis(trimethylsilyl)silane ($C_{12}H_{36}Si_5$; Stream Chemicals Co.) is used as the silicon doping compound. $C_{10}H_8$-$CF_{1.1}$-$C_{12}H_{36}Si_5$ ternary homogeneous mixture with a Si:C atomic ratio of 0.07 is used as the initial material for diamond synthesis. The tablets (5-mm diameter and 4-mm height) of cold-pressed starting mixture are placed in a graphite container that simultaneously serves as a heater of the high-pressure "toroid"-type apparatus. The experimental procedure consists of loading the high-pressure apparatus to 8 GPa at room temperature, heating the sample to the desired temperature (approximately 1200 °C), and isothermal exposure of the sample for 20 s at this temperature. The high-pressure states obtained are isolated by quenching to room temperature under pressure and then complete pressure release. The recovered diamond materials are characterized under ambient conditions by X-ray diffraction, Raman spectroscopy, scanning electron microscopy (SEM), and transmission electron microscopy [21].

B. Size selection of NDs

After production the NDs are not size selected and range in size from nanometers to a few micrometers. To size

select them, centrifugation is used. The NDs, which are in a solution of ethanol and micro water, are dispersed in 1 ml of micro water, which is then centrifuged at 2000 revolutions/min, and the liquid at the top is transferred to a new container. The liquid removed contains the smallest NDs of the original mixture, the ones used for the experiments described here.

The remaining NDs in the condensed liquid are diluted again with 1 ml of micro water and the process of dilution and centrifugation is performed another 3 times at 1000, 500, and 300 revolutions/min to obtain solutions with NDs of different sizes. As the ND concentration of each liquid with the size-selected NDs is low after this process, all new solutions are centrifuged at 5000 revolutions/min and the liquid at the top of each solution is removed and stored in a separate container. The concentrated solution that is obtained by centrifugation at 2000 revolutions/min contains the smallest NDs, most of which are about or smaller than 130 nm when observed by SEM on the same type-IIa-diamond substrate as used in cryogenic measurements. For the minority NDs, the ND size, when observed by SEM, ranges from 30 to 280 nm. The resolving power of microscopy is constrained by the surface charging of the nonelectroconductive diamond substrate, leading to poor image quality for NDs smaller than 30 nm. For larger-sized anomalies, over many SEM sessions, only three NDs larger than 200 nm were found.

C. H-plasma treatment

The surface termination is done in a plasma-assisted-chemical-vapor-deposition reactor. The microwave cavity is formed by a glass cylinder in which the microwave antenna is placed and a movable sample plate, on which the NDs on a single-crystal type-IIa diamond are mounted. The chamber is pumped to a vacuum of 10^{-10} mbar before the process begins. Hydrogen at a flow rate of 300 sccm is pumped into the reactor, whereby the pressure is increased stepwise to 25 mbar over 480 s. In the same time, the microwave power and the temperature are increased, also stepwise, to 2.5 kW and 750 °C, respectively. To stabilize the plasma, the resonator height is adjusted and the microwave back reflection is set to a minimum, by optimization of the microwave conductor manually. These conditions are maintained for 60 s before all parameter values are decreased stepwise to zero in 390 s. During this whole time the NDs are exposed to the plasma, which results in a hydrogen surface termination.

D. Cryogenic confocal microscopy and sample preparation

For the lowest background fluorescence and greatest thermal conductivity, a type-IIa diamond is chosen as the substrate material (2×2 mm^2). Markers are etched into the surface with selective carbon milling by a Helios 3D FEG instrument. Substrates are cleaned in a boiling solution (approximately 100 °C) of $HClO_4$-H_2SO_4-HNO_3. The untreated ND solution is diluted with chloroform and placed in an ultrsonic bath for 10 min. Then 2 μl of the diluted sample is spin coated onto the substrate at 5000 revolutions/min for 40 s.

The sample is mounted on the cold finger of a continuous-flow helium cryostat, which is cooled to 8 K for imaging with a homebuilt confocal microscope. Experimental control is provided by the QUDI software suite [22]. The Si-V^- centers are off-resonantly excited by a 532-nm laser of 120 ± 10 μW in front of the objective lens. Spectra are measured after a 560-nm long-pass filter, and polarization dependence is measured by rotation of the fluorescence with a half-wave plate before recording of the spectra through a fixed Glan-Thompson polarizer. This prevents any polarization dependence of the detection instruments from impacting the results. Statistical processing of spectra is performed by Bayesian inference (see Appendix C for details), and the PYTHON packages EMCEE [23] and PyMC and PyMC3 [24] are used to perform the computations with the Markov-chain Monte Carlo (MCMC) ensemble sampler. Resonant-excitation and lifetime-stability measurements are performed for power-broadened lines to increase the signal-to-noise ratio, thereby increasing the reliability of the data.

E. AFM positioning procedure

Before positioning, the ND region is imaged in the AFM and a reference ND is selected. The positions of other NDs are quickly estimated from visual inspection of the topographic image, and a pushing distance is determined. The ND is moved with use of the AFM tip in contact mode; the exact mechanics of this process depend on the shape of the AFM tip and the ND and the nature of their contact. It is possible for the ND to deviate sideways in undesired directions over the course of the movement, and it is important to avoid pushing the ND over the desired location. The positioning accuracy may be improved by further cycles of position measurement and fine positioning as well as two-dimensional Gaussian fitting (see below) of the position of the ND at every step; however, this is not done here for two reasons: first, the single-shot positioning accuracy is sufficient for many applications relying on optical coupling; second, this single-shot procedure gives a useful lower bound on the nanomanipulation accuracy and is a valuable reference for further comparison.

After nanomanipulation, the ND positions are obtained with more precision by our fitting each ND spot with a circular two-dimensional Gaussian function. The full width at half maximum (FWHM) is about 75 nm, but the excellent height resolution of the AFM makes it possible to locate the Gaussian fit within about 1 nm. Additional uncertainty arises from the fact that NDs are not circularly symmetric

(leading to an effective offset of the Gaussian fit). However, these uncertainties are considered to be much smaller than the size of the ND, and so their contribution to the emitter-position uncertainty is minimal.

The uncertainties in the calculated magnitude and angle of the magnetic field are a direct result of the 1-MHz uncertainty in the zero-field splitting D. This error is less important for changes in angles or magnetic fields than for the absolute values, as the D-field value does not change for a nitrogen vacancy in between measurements. The uncertainties of the angle and B field are calculated by Gaussian error propagation with the help of the PYTHON package UNCERTAINTIES [25].

III. RESULTS

A. Surface treatment of NDs to alter Si-V^- optical properties

Intrinsic Si-V^- centers form during growth of NDs synthesized by chemical vapor deposition [26] and also by direct HPHT synthesis [21]. The HPHT conditions effectively allow crystal annealing during growth, which can lead to the production of low-strain NDs. HPHT NDs were previously found to host Si-V^- centers with excellent optical properties [19], and these same ND samples are used here. The NDs are size selected with use of a centrifuge (procedure outlined in Sec. II B) and are spin coated on type-IIa-diamond substrates containing markers produced by selective carbon milling [19]. The typical ND size was around or below 130 nm, and the physical dimensions of specific NDs under study are obtained from SEM images that were spatially correlated with fluorescence images with use of the substrate markers.

Previous spectroscopic investigations of Si-V^- centers in these HPHT NDs suggested that the optical properties were impacted and in some ways limited by effects on the ND surface [19]. In particular, the photoluminescence (PL) spectrum of the zero-phonon lines (ZPLs) of Si-V^- centers exhibit undesired spectral diffusion. This is characterized by off-resonant excitation at 532 nm and at a cryogenic temperature of 8 K (apparatus described in Sec. II D), where groups of narrow lines around 737 nm are observed in the PL spectrum as shown in shown in Fig. 2(a). These features in the spectrum arise from the direct optical transitions of Si-V^- centers, and it is apparent that they shift position and sometimes blink over the measurement duration. Our taking the time-averaged emission from these measurements and summing across 15 different spots produced the small-ensemble PL spectrum shown in red in Fig. 2(c). The characteristic four-line pattern of the Si-V^- zero-phonon line [13,27] cannot be resolved, indicating that the inhomogeneous spread of Si-V^- centers in this ensemble is broader than the 252-GHz excited-state splitting. This result is consistent with previous reports [19], and is a fundamental limitation to many applications when continuous resonant excitation of individual optical transitions is required.

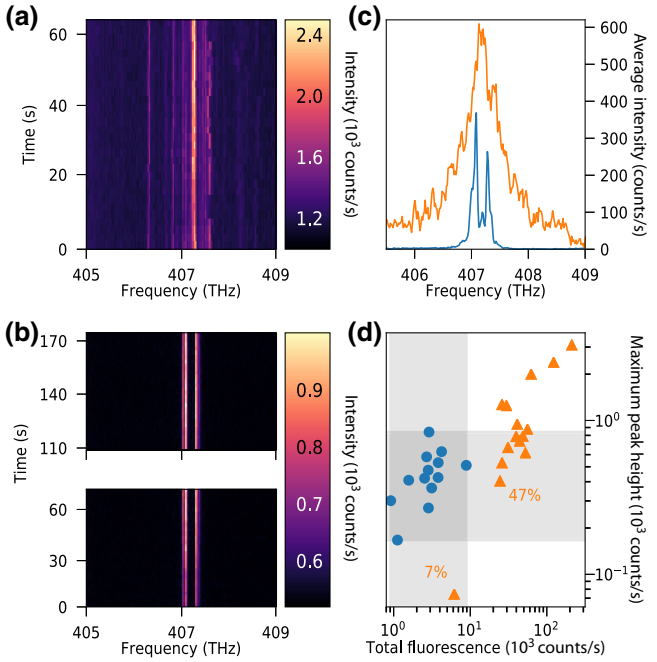

FIG. 2. Comparison of optical properties of untreated and H-plasma-treated Si-V^- in NDs at cryogenic temperature. (a) Time-resolved spectrum of Si-V^- in an untreated ND sample exhibiting many lines and spectral diffusion. (b) Time-resolved spectrum of Si-V^- in a H-plasma-treated ND sample, which exhibits the four-line fine structure of the Si-V^- ZPL, with no spectrometer-resolvable spectral diffusion. The discontinuity of time between 70 and 110 s is due to refocusing of the confocal microscope. (c) The broader, orange spectrum (15 spots) is the inhomogeneous spectrum from untreated ND samples. The narrower, blue spectrum, where doublet-like fine structures can be resolved, is the inhomogeneous spectrum of spectrally stable points from H-plasma-treated ND samples (23 spots). (d) Comparison of the total fluorescence and maximum peak height for spots in the H-plasma-treated (blue circles) and untreated (orange triangles) samples. The shaded regions illustrate that the H-plasma treatment reduces the total fluorescence much more than the height of individual peaks in the spectra. Only 7% of spots from the untreated sample have total fluorescence overlapping with total fluorescence from treated-sample spots, while 47% of the points from the untreated sample have a maximum peak height in the same range as points from the H-plasma-treated sample.

Part of this ND sample is treated in a hydrogen plasma (see Sec. II C), and time-resolved PL spectra are measured for 23 spots containing Si-V^-. The PL spectra of Si-V^- transitions in the treated NDs show significantly improved spectral stability; a typical measurement is shown in Fig. 2(b). In addition, the four-line fine structure of Si-V^- is clearly visible in the PL spectrum for 17 of the 23 points investigated (see Appendix B). For two points we observe broader spectral peaks in a stable doublet, which may be attributed to a thermal broadening of the peaks

with higher temperatures due to small contact area between those NDs and the substrate. The small-ensemble spectrum [blue curve in Fig. 2(c)] integrated for the stable spectra in the treated sample clearly has a doublet structure, indicating that the inhomogeneous distribution is narrower than the 252-GHz excited-state splitting.

We compare the PL spectra from the treated sample with the PL spectra from the untreated sample at cryogenic temperature and with identical experimental settings. As shown in Fig. 2(d), there is only a minor effect on the maximum peak height causes by H termination, as 47% of the points from the untreated sample lie in the same range as the points from the H-plasma-treated sample. In contrast, the total fluorescence altered significantly (within the range between 733 and 741 nm), with an overlap quantity of only 7%. This indicates that the surface treatment reduces the brightness of the NDs by "switching off" some of the Si-V^- centers, but the remaining ones are just as bright as they were before treatment. If more than one emitter is present in a focal spot, overlapping emission lines could lead to a change in the maximum peak height in a spectrum. However, the large inhomogeneous spectral distribution in the untreated NDs suggests a small likelihood of overlapping emission lines between Si-V^- centers in any given ND. In addition, Si-V^- centers in untreated NDs give a $g^2(\tau)$ autocorrelation function with no visible dip at $\tau = 0$ (the signature of single quantum emitters), whereas Si-V^- fluorescence from the treated NDs shows clear sub-Poissonian emission with $g^2(0)$ down to 0.2 after background correction (see Appendix A). This strengthens the interpretation that the surface treatment has reduced the number of active Si-V^- centers in the NDs, and indicates the possibility to isolate single Si-V^- center that are spectrally very stable per ND even under off-resonant excitation.

B. Strain analysis of the fine structure of Si-V^- in NDs

Variation in the ZPLs between NDs is attributed primarily to differences in strain. The ^2E_g ground state and ^2E_u excited state each have twofold orbital degeneracy, and are intrinsically split by spin-orbit interaction as illustrated in the inset in Fig. 1 [27]. Strain aligned with the symmetry axis of the Si-V^- center does not lower the symmetry and so cannot lift the orbital degeneracy, but it can shift the energies of the ground and excited states, and this appears as a shift in the position of the ZPL. Strain transverse to the symmetry axis does lift the orbital degeneracy, splitting the E_x and E_y orbitals apart in energy. This is observed as an increase in the splitting between fine-structure peaks in the ZPL, which are resolved in the cryogenic PL spectrum as shown in Fig. 3(a). The ZPL position and the splittings for ground and excited states are determined for each Si-V^- that showed a clear four-line spectrum. Figure 3(b) shows the position versus the ground-state splitting, which essentially corresponds to axial strain versus transverse strain. There is no correlation, which is consistent with a random orientation of the strain in the NDs relative to the Si-V^- symmetry axis. This comparison is further complicated by the numerous unrelated effects such as temperature [28] and isotopic shift [29] that can shift the Si-V^- transitions (but not cause splitting). It is, however, apparent that almost half of the Si-V^- transitions are clustered fairly close together near the minimum ground-state splitting [shaded in Fig. 3(b)]. Spectral splitting indicates splitting of the orbital degeneracy in the E ground and excited states. Unlike the line position, transverse strain is the most likely cause of orbital splitting, and so the spectral splitting can provide more information about strain.

The transverse strain is modeled for the four-level system illustrated in the inset in Fig. 1 with use of the standard strain Hamiltonian

$$\begin{pmatrix} \nu + \frac{1}{2}\lambda^e_{\mathrm{SO}} & \delta E^e & & \\ \delta E^e & \nu - \frac{1}{2}\lambda^e_{\mathrm{SO}} & & \\ & & \frac{1}{2}\lambda^g_{\mathrm{SO}} & \delta E^g \\ & & \delta E^g & -\frac{1}{2}\lambda^g_{\mathrm{SO}} \end{pmatrix}, \quad (1)$$

where ν is the optical transition frequency (ZPL position), λ^e_{SO} and λ^g_{SO} are the spin-orbit splittings in the excited state and the ground state, respectively, and δE^e and δE^g are the strain splitting coefficients in the excited state and the ground state, respectively. Fitting of the acquired four-line spectra to our model using Bayesian inference yields a strong correlation between the excited-state splitting and the ground-state splitting [Fig. 3(c)]. This is expected for transverse strain, which must be the same for ground and excited states of a localized Si-V^- center. The correlation between ground- and excited-state splittings in Fig. 3(c) gives the strain coefficient ratio $\delta E^e/\delta E^g = 1.688^{+0.008}_{-0.008}$. Only one study has reported uniaxial strain measurements on Si-V^- centers in diamond [30].

Although the calibration of the strain is unknown in these NDs, the systematic observation of splittings enables reliable identification of the intrinsic Si-V^- spin-orbit splitting. Bayesian inference [31,32] is used to find the most-plausible λ^e_{SO}, λ^g_{SO}, $\delta E^e/\delta E^g$, and strain values for the Si-V^- spectra. The use of Bayesian inference allows the many-dimensional model to be used effectively, and avoids the complications of calculating uncertainty propagation with non-Gaussian errors (for more details, see Appendix C). The results are illustrated in Fig. 3(d), and give zero-strain splittings $\lambda^g_{\mathrm{SO}} = 46.3^{+2.5}_{-3.4}$ GHz and $\lambda^e_{\mathrm{SO}} = 252.0^{+1.3}_{-1.8}$ GHz for the ground state and the excited state, respectively (the full posterior distributions are given in Appendix C). These results also indicate that 13 of the 18 Si-V^- spectra are in the "low-transverse-strain" region, where the splittings are dominated by spin-orbit interaction

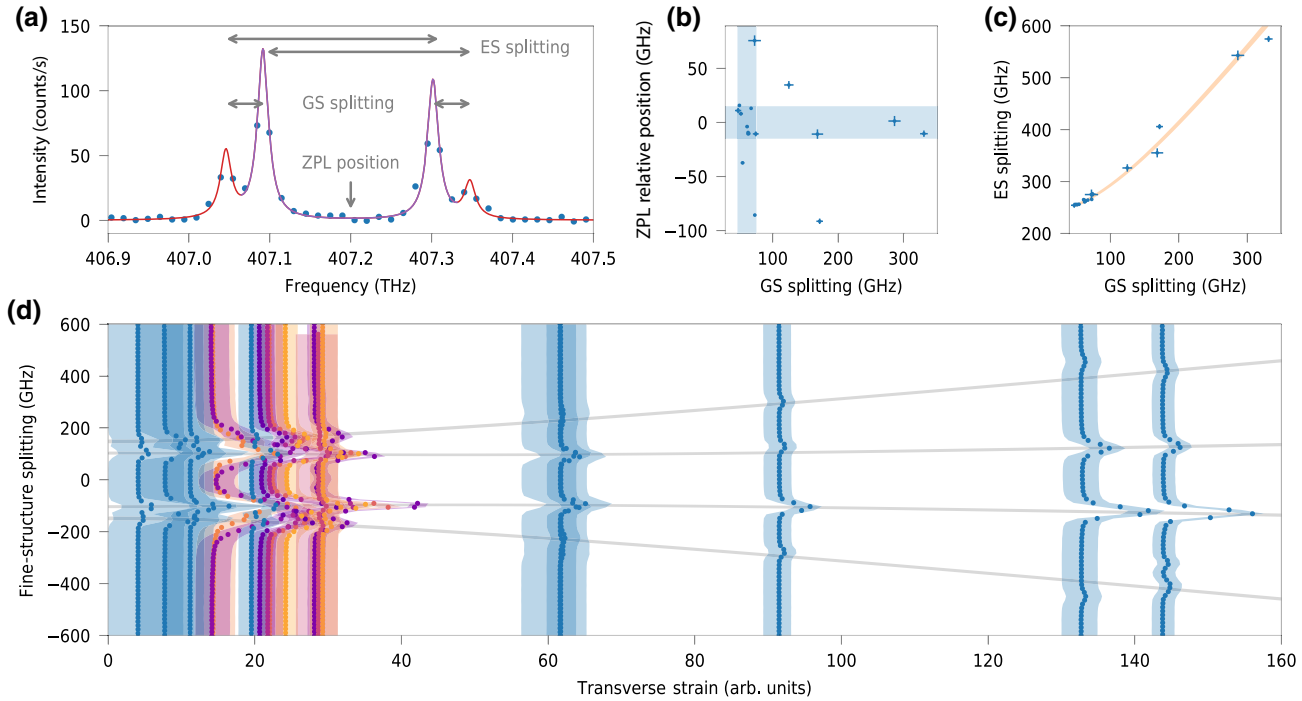

FIG. 3. Strain analysis of Si-V^- centers in the nanodiamond environment. (a) The four optical transitions A, B, C, and D (see Fig. 1) are resolved at low temperature in the PL spectrum. Transverse strain increases the ground-state (GS) and excited-state (ES) splittings, and axial strain (along with other factors) can alter the ZPL position. (b) The four-line PL spectrum is clearly identified in 17 of the 23 spots measured, and the splittings are determined. There is no correlation between the Si-V^- ground-state splitting and the ZPL central frequency due to the random orientation of strain in the NDs. The shaded region (30 GHz horizontally and vertically) is interpreted as low strain and contains eight of the 17 NDs. (c) There is close correlation between ground-state splitting and excited-state splitting. The orange region represents the 95% credible region inferred from a transverse-strain model, and these data indicate that the excited-state strain-splitting coefficient is $1.688^{+0.008}_{-0.008}$ times larger than that of the ground state. (d) Statistical inference of the Si-V^- strain splitting from 18 PL spectra (a spot with an unresolved four-line pattern is suitable for this analysis). The gray lines represent the 95% credible region for the optical transition energies split by transverse strain, and provide a systematic identification of the Si-V^- zero-field splittings in the ground ($46.3^{+2.5}_{-3.4}$ GHz) and excited ($252.0^{+1.3}_{-1.8}$ GHz) states. Each spectrum is placed at its inferred transverse-strain value, with the shaded band corresponding to the 95% credible region. The spectra between 14 and 30 strain units are colored to aid visual differentiation. Thirteen of the Si-V^- spectra correspond to the low-transverse-strain situation, where the splitting is dominated by spin-orbit interaction (increasing the chances of spectrally identical emitters).

(below about 40 transverse strain units). It is remarkable to find such a high proportion of low-strain Si-V^- centers in small NDs.

C. Recovery of spectral bulk properties

Resolving the fine structure also provides an opportunity to study the polarization behavior of single Si-V^- centers in NDs. In the absence of perturbations such as strain, the four optical transitions of the Si-V^- ZPL are known to follow the polarization rules illustrated in Fig. 1 [27]. Lines B and C arise only from the dipole moment parallel to the Si-V^- axis (z), and have strong polarization contrast. Lines A and D arise from the perpendicular x, y dipole moments, and the viewing geometry means that these always appear "polarized perpendicular" to lines B and C (although lines A and D typically show less polarization contrast because they are not from a single dipole). Polarization dependence of the spectrum is recorded for many of the Si-V^- sites found in NDs, and a typical example is shown in Fig. 4(a). The polarization behavior is the same as for Si-V^- in low-strain bulk diamond. This adds further support to the interpretation of minimal strain for these Si-V^- centers in NDs, and also demonstrates access to experiments in a cross-polarized configuration.

Related work has shown that Si-V^- centers in nanodiamonds can have nearly-lifetime-limited emission [19]. For an indistinguishable photon source, it is furthermore important to establish spectral stability within the range of lifetime-limited linewidth for sufficiently long time. A set of 19 photoluminescence excitation (PLE) scans are recorded sequentially in 600 s. In six of these scans the Si-V^- blinks off while the peak is scanned, leading to misfits of the peak position. The resonance frequencies of the remaining 14 scans are scattered within a frequency band of 108 MHz. This PLE measurement is far more

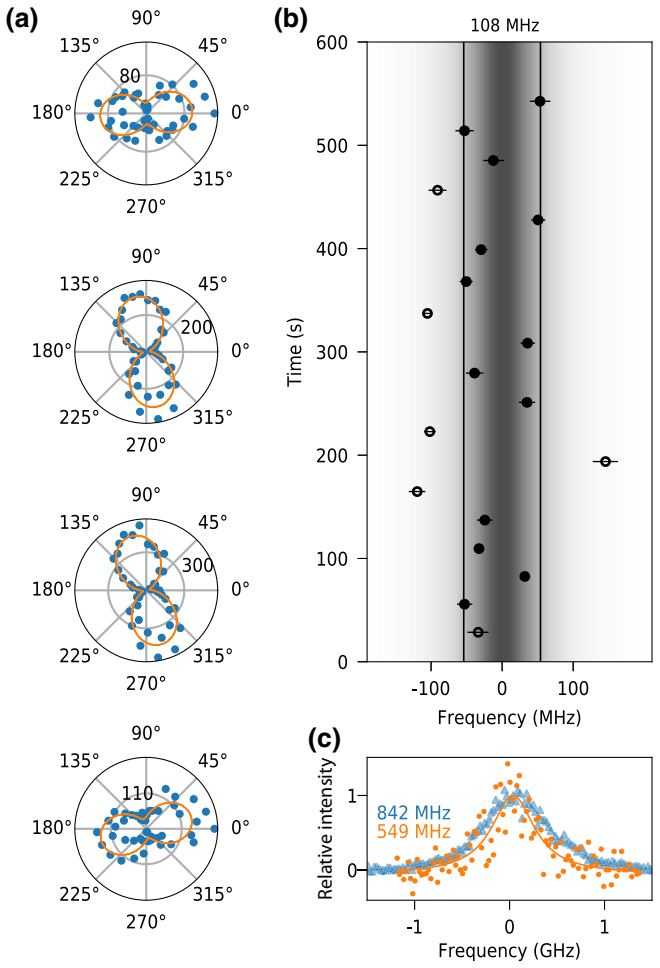

FIG. 4. Polarization of ZPL and spectral stability under resonant excitation of Si-V^- in H-plasma-treated NDs. (a) The polarization pattern of the four-line fine structure for optical transitions A, B, C, and D (from top to bottom). The expected behavior of low-strain bulk Si-V^- can be recovered. (b) Line position of a resonantly excited Si-V^- center over 600 s. Occasional blinking destroys the symmetry of some PLE scans, resulting in ill-fitted peak position (open circles). Excluding such points, the transition frequency remains inside a range of 108 MHz, as indicted by the shaded band. (c) The average PLE linewidth (blue triangles) is 842 MHz and the narrowest scan (orange circles) has a width of 549 MHz. The peak heights are normalized to 1 for better comparison.

precise than the spectrometer-resolved data in Fig. 2. An excited state lifetime of 1.5 ns is extracted from $g^2(\tau)$-autocorrelation-function measurements (see Appendix A), corresponding to a lifetime-limited linewidth of 106 MHz. It is concluded that the surface treatment is able to recover excellent spectral stability.

Although the line position is found to be stable within the lifetime-limited linewidth, the PLE linewidths for each of these scans are broader. The narrowest peak is at 549 MHz, and the data averaged over all scans have a width of 842 MHz. This makes it impossible to rule out fast spectral instability on a timescale much shorter than the PLE scan period, but there are other effects that also account for this broadening. The PLE measurement is made on Si-V^- transition C with an excitation power of 600 nW at the objective, which is 10 times higher than for similar measurements previously performed on Si-V^- centers in bulk diamond samples. It is also difficult to be sure of the temperature of NDs, which have less reliable thermal contact with the cryostat cold finger than bulk samples typically achieve. Thermal broadening of the transition would account for the need to use higher laser power in PLE scans, and the use of higher laser power may have caused additional power broadening.

D. Manipulation of NDs on the nanoscale

Positioning NDs containing negatively-charged-nitrogen-vacancy (N-V^-) centers in close proximity to plasmonic structures and within the electromagnetic field mode of a photonic crystal cavity was demonstrated with an AFM [16,18,20]. In these studies the positioning precision was determined from the coupling strength to the photonic structure under investigation. Here we perform position manipulation of NDs on the nanoscale with previously unachieved accuracy using an AFM in high-resolution contact mode and introduce manipulation tools, such as dipole rotation and ND declustering. Small NDs with an average diameter of 25 nm are chosen since the diamond size fundamentally limits the uncertainty of localizing the emitter in a confocal microscope. The NDs are preselected to contain N-V^- centers, since these provide a well-established way to spectrally determine alignment angles to an external magnetic field [33]. The N-V^- centers are imaged with an integrated confocal fluorescence microscope.

A string of four NDs is aligned and equally spaced with 1.5-μm separation as shown in Fig. 5(a). The confocal-fluorescence-microscopy images show that bright NDs are moved into a straight-line configuration. The AFM lateral resolution is limited by the cantilever-tip radius of curvature (nominally approximately 10 nm), and is capable of imaging spots of about 75-nm width (FWHM). This is considerably lower than the diffraction-limited confocal-microscope resolution. The final position coordinates of the NDs are obtained from the center of the two-dimensional Gaussian fits to the AFM topographic data. The typical deviation of the ND positions from the target coordinates is $\Delta x_{nn} = 37$ nm and $\Delta y_{nn} = 22$ nm, where n represents the index of the ND.

On our device, the pushing operation requires a "field of view" that includes the reference position as well as the desired position. Measurements of separation distances are less precise for a wider-field scan, and so the ND positioning accuracy diminishes with increasing separation from the reference location. ND separations much larger than

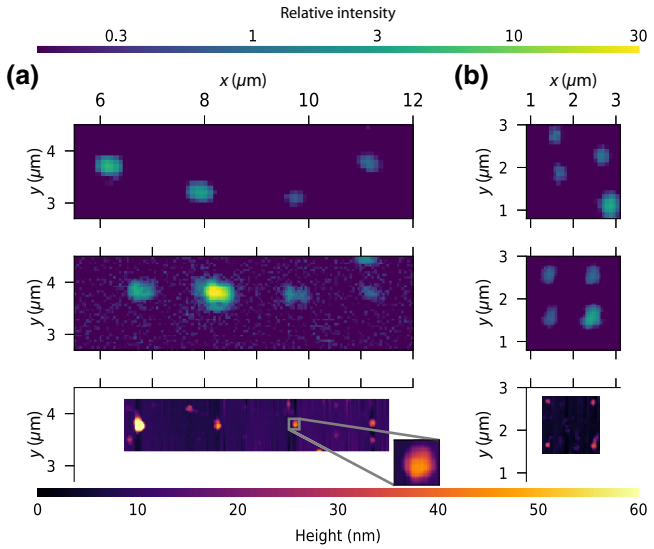

FIG. 5. Manipulation of NDs at the nanoscale. (a) One-dimensional alignment of four NDs with an accuracy of 37 nm. From top to bottom, fluorescence image of a spin-coated ND sample on glass, fluorescence image of the same sample area after nanopositioning with the AFM in contact mode, and topography image of the aligned four-ND string with the ac mode of the AFM. The intensity of fluorescence of emitters is plotted logarithmically, and is normalized by the fluorescence intensity of the unmoving ND (far right) for better visual recognition of the spatial positions. The inset spans 0.2×0.2 μm^2 to illustrate the AFM resolution, which has a full width at half maximum of 75 nm. (b) Two-dimensional nanopositioning with accuracy of 37 nm. From top to bottom, fluorescence image of a spin-coated ND sample on glass, fluorescence image after nanopositioning of AFM in contact mode, and topography image of the aligned four-ND square with ac mode of the AFM. The color bars are shared between (a) and (b).

the optical wavelength are chosen here to extract a lower bound on the positioning accuracy.

Two-dimensional arrays of NDs are more challenging to align but are of great interest for many applications. This capability is demonstrated by our arranging a different set of four NDs into a square pattern with separation of 1 μm as shown in Fig. 5(b). The position deviation from the target coordinates is similar to that observed for the straight-line arrangement, but increased slightly for the corner diagonally opposite the reference ND due to the successive positioning procedures. All positioning operations are performed with a precision on the order of the ND size, and further precision may be obtained by iterating the procedure with feedback from intermediate measurements of the ND location (see Sec. II E). The location of the N-V^- or Si-V^- emitter within a ND is difficult to obtain, and this represents a fundamental limit on the positioning accuracy of the emitter. We estimate the overall position uncertainty of the emitter is approximately 40 nm, where the size of the ND is the dominant contributing factor.

Optically detected magnetic resonance (ODMR) is measured for a single N-V^- center in one ND. With this measurement, information on the alignment of the N-V^- center relative to a stationary external magnetic field from a 3-mm magnet cube situated about 8 mm from the NDs is acquired. The magnet creates a field of 39 ± 4 G at the measured ND. The observed resonance frequencies of 2834.8 ± 0.1 MHz and 2913.8 ± 0.2 MHz [Fig. 6(a), uncertainties deduced from Lorentz fitting] correspond to an angle of $69^\circ \pm 2^\circ$ between the N-V^- symmetry axis and the magnetic field. This ND is moved approximately 100 nm, and the ODMR resonance frequencies are changed to 2788.3 ± 0.1 MHz and 2954.0 ± 0.1 MHz, corresponding to an angle of a $38^\circ \pm 6^\circ$ relative to the external field. It is concluded that the manipulation rotated the ND by approximately $31^\circ \pm 5^\circ$, which demonstrates a potential dipole-alignment procedure by rotational ND manipulation. The calculation of the magnetic field as well as the angle between the N-V^- symmetry axis and the magnetic field using ODMR frequencies of N-V^- centers is done according to Ref. [33]. The comparatively large uncertainties in the angle arise mainly from the fact that the zero-field splitting is known to a precision of only ± 1 MHz [34] at room temperature. For more-precise final alignment, an order-of-magnitude improvement would be possible if the zero-field splitting were measured for the specific N-V^- center under investigation (see Sec. II E for details).

NDs commonly form clusters when they are dispersed on a substrate, and various techniques have been developed to discourage this phenomenon. We perform a topological

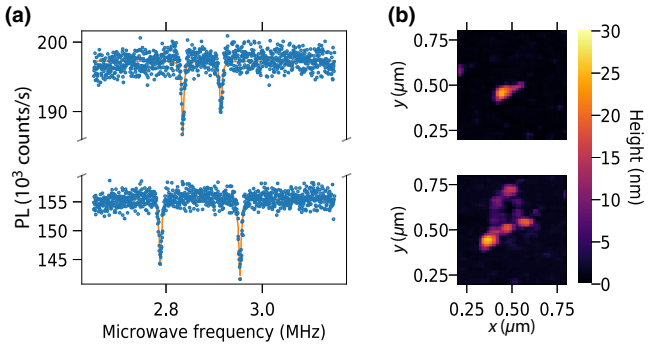

FIG. 6. *In situ* manipulation of NDs. (a) Demonstration of nitrogen-vacancy axis rotation during one tip push with the AFM in contact mode with a pushing distance of approximately 100 nm in a constant magnetic field. Before the rotation (top) the resonant frequencies are 2834.8 ± 0.1 MHz and 2913.8 ± 0.2 MHz, corresponding to 39 ± 4 G and the angle between the nitrogen-vacancy axis and the magnetic field $\theta = 69^\circ \pm 2^\circ$. After the rotation (bottom) the resonant frequencies are 2788.3 ± 0.1 MHz and 2954.0 ± 0.1 MHz, corresponding to 38 ± 4 G and an angle $\theta = 38^\circ \pm 6^\circ$. (b) Decomposition of a ND cluster. Larger clusters of ND (top) can be decomposed by pressing the AFM cantilever into the cluster (bottom).

scan of such a ND cluster and show that it is possible to decompose a cluster after it has formed on a substrate by our pushing the AFM cantilever into it. In Fig. 6(b) a typical cluster found in our sample is shown as a topological scan. After our pushing the tip into the sample, many new features appear in the scan with sizes that are expected for single crystals. It is apparent that manipulation with the AFM tip is capable of decomposing a ND cluster into its individual components.

IV. DISCUSSION

While it is significant that the H-plasma treatment alters the spectral properties of Si-V^- centers in these NDs, the mechanism for this change is less obvious. For N-V^- centers it has been suggested that the strong band bending leads to holes being created in the valence band by H-plasma surface termination and absorption of H_2O [35]. Such discharge of the emitters close to the surface for plasma-treated NDs containing Si-V^- centers could lead to a reduction of the overall fluorescence as observed, and consequently, only emitters with larger distance to the diamond surface would remain active. These are likely to be the least-strained Si-V^- centers in the NDs, and so this explanation accounts for the reduction in inhomogeneous ensemble linewidth and the high incidence of low-strain spectra. It is also possible that the more-highly-strained Si-V^- centers are more susceptible to the discharging effect of the surface termination.

The reduction or elimination of spectral diffusion is significant because part of the interest in Si-V^- centers arose from the absence of spectral diffusion in low-strain bulk diamond [11]. Until now the desirable atomlike spectral properties were only reported for Si-V^- centers in bulk diamond, although recently they were also seen for Si-V^- centers in nanostructured diamond waveguides [36], leading to entanglement of two Si-V^- centers [10]. The degradation of optical properties is problematic in particular for Si-V^- centers in small NDs with diameter less than 100 nm that are desired for hybrid approaches due to low light scattering and precise positioning capabilities. Spectral diffusion is a particular problem for the application in arrays of emitters, since inhomogeneity in spectral properties limits the optical coupling between nodes in the array. This has been a substantial problem for arrays of N-V^- centers created through ion implantation and subsequent annealing, and magnetic coupling has been demonstrated [37,38].

While it is possible to prepare NDs containing both N-V^- and Si-V^- centers, an alternative nanomanipulation protocol could be realized for NDs containing only Si-V^- centers. Only the dipole alignment would require an alternative method. The high optical polarization contrast shown in Fig. 4(a) could be iteratively measured to achieve the desired rotational orientation without requiring N-V^- centers and external magnetic fields. In the development of Si-V^- arrays, such rotational manipulation is important to allow the alignment of optical dipoles for optimum coupling.

Since the position of NDs is determined from two-dimensional Gaussian fits, the uncertainties will increase with ND size. This can be partially solved by intermediate fitting steps, with the penalty of decreased speed of the manipulation process. At the end, the most-important position accuracy is that of the location of the quantum emitter, which is then limited only by the size of the NDs. For improved super-resolution of the emitter position beyond the size of the ND, other techniques, such as stimulated-emission-depletion microscopy, could be used [39].

V. CONCLUSION

In this work we experimentally demonstrate how to recover symmetry-protected optical transitions of Si-V^- centers in low-strain NDs. Together with manipulation capabilities of NDs on the nanometer scale, our work opens alternative routes for bottom-up assembly of indistinguishable quantum-emitter arrays and nanophotonic devices with deterministic coupling and emitter position control much better than the diffraction limit. Individual NDs with diameter around 100 nm contain single Si-V^- centers with bulklike spectral stability. Such small NDs are most suitable for hybrid technology due to minimized light scattering and high positioning precision. Furthermore, a diamond host with dimensions less than 100 nm introduces a cutoff frequency in the phonon density of states beyond 50 GHz. The spin coherence time of Si-V^- centers in bulk diamond is limited to approximately 100 ns at 4 K due to interaction with acoustic phonons at a frequency corresponding to the ground-state splitting of approximately 50 GHz [28,40–43]. Our work enables, therefore, investigation of prolonged spin-coherence times of Si-V^- centers in NDs at moderate temperatures. So far, an extended spin-coherence time T_2 of 13 ms and a spin-relaxation time T_1 exceeding 1 s in the bulk have been demonstrated at a temperature of 100 mK in a dilution refrigerator [44].

Furthermore, the measurement of the zero-field strain splitting can be used to find the relative transverse strain for Si-V^- centers both in bulk diamond and and nanodiamonds and as a gauge for optomechanical experiments with Si-V^- centers [45].

ACKNOWLEDGMENTS

We acknowledge G. Neusser and the FIB Center UUlm for etching the markers into the type-IIa-diamond substrate. We acknowledge help from F. Frank (University of Ulm) with the AFM, A. Gilchrist (Macquarie University) for guiding discussions in developing the Bayesian

analysis, and S. Strehle (Institute of Electron Devices and Circuits, University of Ulm) for experimental support. L.R. is a recipient of an Australian Research Council Discovery Early Career Award (Project No. DE170101371) funded by the Australian Government. V.A.D. thanks the Russian Foundation for Basic Research (Grant No. 18-03-00936) for financial support. Y.L. is currently supported by the Sino-German (CSC-DAAD) Postdoc Scholarship Program (Grant No. 57251553). A.B.F. acknowledges support of the Carl-Zeiss Foundation. F.J. acknowledges support of the DFG, BMBF, VW Stiftung, and EU (ERC, DIADEMS). A.K. acknowledges the generous support of the DFG, the Carl-Zeiss Foundation, IQST, and the Wissenschaftler-Rückkehrprogramm GSO/GZS.

The experiments were conceived by L.J.R., A.K., and F.J. O.W., A.B.F., and L.J.R. performed the spectroscopic measurements. O.W. and C.O. performed the surface treatment. Y.L. and L.A. nanomanipulated the nanodiamonds. A.B.F. and O.W. prepared the samples. A.B.F. preformed the SEM measurements. L.J.R. and O.W. performed the Bayesian strain analysis. V.A.D. and V.N.A. synthesized the NDs with Si-V^- centers. The manuscript was written by O.W., A.B.F., L.J.R., and A.K., and all authors discussed the results and commented on the manuscript.

L.J.R. and O.W. are the two equally contributing, first authors of the manuscript.

APPENDIX A: $G^2(\tau)$-AUTOCORRELATION-FUNCTION MEASUREMENT

$g^2(\tau)$-autocorrelation-function measurements are conducted to confirm the existence of single Si-V^- emitters in ND and extract the lifetime of the excited state. Measurements are performed in a Hanbury-Brown-Twiss setup at cryogenic temperature (8 K) with off-resonant excitation.

Figure 7(c) shows a $g^2(\tau)$ autocorrelation function measured on a Si-V^--containing ND, whose PL spectrum [see Fig. 7(a)] shows the typical four-line ZPL pattern at cryogenic temperature.

The measured $g^2(\tau)$ data are fitted to a two-level model, given by

$$g^2(\tau) = 1 - ae^{-\frac{|\tau|}{\tau_1}},$$

where τ is the delay time and τ_1 is the lifetime of the excited state. The lifetime of the excited state is extracted as $1.5^{+0.6}_{-0.5}$ ns (95% credibility). Following the method of background correction from Ref. [46], we estimate the signal-to-background ratio to be 0.55 by fitting the density plot from the confocal-microscopy scan in Fig. 7(b) to a two-dimensional Gaussian peak. The background-subtracted $g^2(\tau)$ shows a dip below 0.5, an indication of a single emitter.

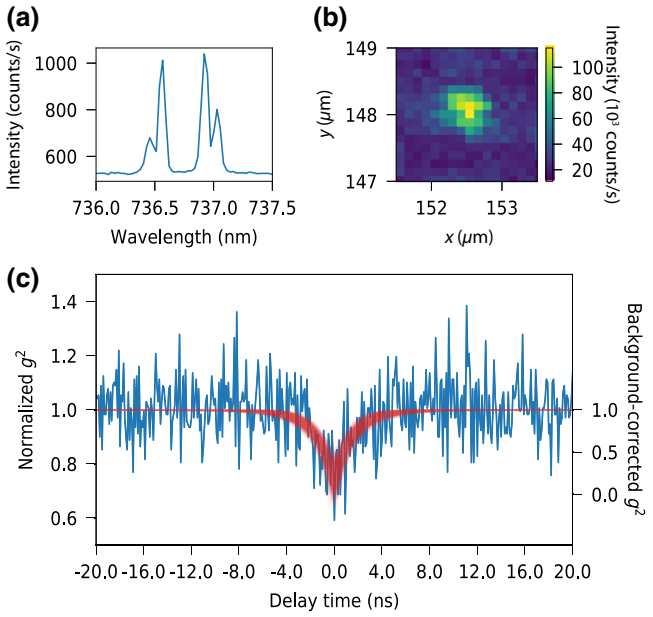

FIG. 7. $g^2(\tau)$-autocorrelation-function measurement shows the existence of single Si-V^- emitters in ND. (a) PL spectrum of the measured single Si-V^- site. (b) Confocal-microscopy image of the measured Si-V^- site. (c) Normalized $g^2(\tau)$ autocorrelation function. Measurement data are shown in blue, while the 95% credible region of the Bayesian inference is plotted as red shading. The y axis on the left shows normalized values without background correction, while the y axis on the right shows the value of $g^2(\tau)$ after background correction.

APPENDIX B: POSTSELECTION OF MEASURED PHOTOLUMINESCENCE SPECTRA

For the untreated sample, 15 PL spectra are acquired. All of them are used for Fig. 2 [one spectrum for Fig. 2(a), all 15 for Figs. 2(c) and 2(d)]. PL spectra of 23 spots from the H-plasma-treated sample are measured, and according to the different spectral behavior, subfractions of such spots are used for different analyses. To clarify the use of the measured points from the H-plasma-treated sample in different parts of analysis in this paper, as well as for better understanding of the quality of color centers in the NDs, we list all 23 spots in Table I together with brief descriptions of how they contribute to different evaluations.

The requirements for the different analyses are as follows:

(a) Figure 2(c), treated sample: stable emission of measured spots (22 of 23).

(b) Figure 2(d), comparison of optical properties between treated and untreated samples: Identical experimental settings for the PL spectra of the treated and untreated samples. This means only spectra that are not recorded for polarization measurement (no half-wave plate and Glan-Thompson polarizer in front of the spectrometer)

TABLE I. List of spots with measured PL spectra of the treated sample and their contribution to figures in the manuscript.

Spot number	Contribution	Description
1	Figures 2(c), 2(d), and 3(c)–3(e)	Clear four line
2	Figures 2(c) and 2(d)	Multisite
3	Figures 2(c) and 2(d)	Multisite
4	Figures 2(c), 2(d), and 3(c)–3(e)	Clear four line
5	Figures 2(c), 2(d), and 3(e)	Doublet, single site
6	Figures 2(b)–2(d) and 3(c)–3(e)	Clear four line
7	Figures 2(c) and 2(d)	Doublet, small features around doublet
8	Figures 2(c), 2(d), and 3(c)–3(e)	Clear four line
9	Figures 2(c), 2(d), and 3(c)–3(e)	Clear four line
10	Figures 2(c), 2(d), and 3(c)–3(e)	Clear four line
11	Figures 2(c), 2(d), and 3(c)–3(e)	Clear four line
12	...	Unstable emission, not clear if Si-V^-
13	Figures 2(c), 2(d), and 3(c)–3(e)	Clear four line
14	Figures 2(c), 2(d), and 3(c)–3(e)	Clear four line
15	Figures 2(c) and 3(c)–3(e)	Clear four line
16	Figures 2(c), 3(b)–3(e), and 4(a)	Clear four line
17	Figures 2(c) and 3(c)–3(e)	Clear four line
18	Figures 2(c) and 3(c)–3(e)	Clear four line
19	Figures 2(c) and 3(c)–3(e)	Clear four line
20	Figure 2(c)	Multisite
21	Figures 2(c) and 3(c)–3(e)	Clear four line
22	Figures 2(c) and 3(c)–3(e)	Clear four line
23	Figures 2(c) and 3(c)–3(e)	Clear four line

can be compared. Thirteen of 23 spots from the treated sample and 15 spots (all) from the untreated sample are used.

(c) Figure 3(c), correlation between ground-state splitting and ZPL position: PL spectra with a clear four-line structure (17 of 23).

(d) Figure 3(d), correlation between ground-state and excited-state splitting: PL spectra of single sites with a clear four-line structure (17 of 23).

(e) Figure 3(e), transverse-strain analysis: single-site spectra (18 of 23).

APPENDIX C: CONSTRUCTION OF THE STRAIN MODEL AND BAYESIAN INFERENCE

1. Model

The positions of the spectral peaks for the Si-V^- fine structure are given by the energy separations between the excited-state and ground-state branches. The four-level Hamiltonian describing the ground and excited states is given by

$$\begin{pmatrix} \nu + \frac{1}{2}\lambda^e_{\mathrm{SO}} + S_A & \delta E^e & & \\ \delta E^e & \nu - \frac{1}{2}\lambda^e_{\mathrm{SO}} + S_A & & \\ & & \frac{1}{2}\lambda^g_{\mathrm{SO}} & \delta E^g \\ & & \delta E^g & -\frac{1}{2}\lambda^g_{\mathrm{SO}} \end{pmatrix},$$

where ν is the optical transition frequency, λ^e_{SO} and λ^g_{SO} are the spin-orbit splittings in the excited state and the ground state, respectively, and δE^e and δE^g are the strain splittings in the excited state and the ground state, respectively. In this slightly simplified picture, S_A is called "axial strain" but it has the effect of shifting the excited state with respect to the ground state and not altering any splitting. This term encompasses all of the indistinguishable physical effects (temperature, axial strain, hydrostatic pressure, etc.) that can shift the spectral lines without altering their pattern.

The excited-state and ground-state strain splittings δE^e and δE^g arise from the same transverse strain (which must be independent of the excitation state of the Si-V^- center). However, the two electronic states can have different splittings, and so we consider the transverse-strain coefficients c^g and c^e that dictate the way the system responds to a transverse strain S_T. It is impossible for us to know the transverse-strain coefficients c^g and c^e absolutely without having knowledge of the strain magnitude in each spectrum. However, we can find the ratio $c^{e/g} = c^e/c^g$.

The ideal signal in the absence of background or noise would be made up of four Gaussian peaks. We take Gaussian line shapes because the spectrometer measurements are instrument limited. For this same reason, the linewidths are the same for each of the four lines, but their amplitudes (A, B, C, D) and positions (ν_A, ν_B, ν_C, ν_D) are different. So we have expected counts c_e as a function of ν

given by

$$c_e = Ae^{-(\nu-\nu_A)^2/2\sigma^2} + Be^{-(\nu-\nu_B)^2/2\sigma^2} + Ce^{-(\nu-\nu_C)^2/2\sigma^2} + De^{-(\nu-\nu_D)^2/2\sigma^2}.$$

The transition frequencies (ν_A, ν_B, ν_C, ν_D) are determined from the Hamiltonian and so depend on λ_{SO}^g, λ_{SO}^e, $c^{e/g}$, S_T, and S_A.

If we disregard the background for now, this expected profile of counts versus optical frequency is sampled by the signal that is counted as discrete photons. The probability of observing a certain signal photon count at a given frequency is the Poissonian sampling distribution around c_e; that is,

$$P(c_s|\nu I) = e^{-c_e}\frac{{c_e}^{c_s}}{c_s!}.$$

This involves c_e and inherits a dependency on the parameters of the four-Gaussian shape, so it is really $P(c_s|\nu ABCD\sigma\lambda_{\mathrm{SO}}^g\lambda_{\mathrm{SO}}^e c^{e/g}S_TS_AI)$. Here I represents all of the knowledge of the system and the experiment that is not otherwise explicitly stated. To prevent underflow errors in computation, we need to consider the log probability:

$$\log P(c_s|\nu ABCD\sigma\lambda_{\mathrm{SO}}^g\lambda_{\mathrm{SO}}^e c^{e/g}S_TS_AI) = -c_e + c_s\log c_e - \log(c_s!). \tag{C1}$$

The background counts are from the CCD and are Poisson distributed around an average background rate β. The probability of a background count c_{bg} is therefore

$$P(c_{\mathrm{bg}}|I) = e^{-\beta}\frac{\beta^{c_{\mathrm{bg}}}}{c_{\mathrm{bg}}!}.$$

This depends on β, and so it is really $P(c_{\mathrm{bg}}|\beta)$. Calculating this is tricky because $\beta^{c_{\mathrm{bg}}}$ and $c_{\mathrm{bg}}!$ are huge, leading to overflows. It is more tractable to consider

$$\log P(c_{\mathrm{bg}}|\beta I) = -\beta + c_{\mathrm{bg}}\log\beta - \log\left(c_{\mathrm{bg}}!\right).$$

Now it is possible to consider the actual posterior distribution. In other words, given a certain set of model parameters, what is the probability of observing a particular count value c? This is slightly complicated, because the observed counts come from the signal and the background, but we do not have any way of knowing the relative contributions. Instead of answering this, we can give the posterior probability as a sum of possible (and mutually exclusive) options. Either we had c signal counts and zero background counts, or $c-1$ signal counts with one background count, or so on.

This gives

$$\begin{aligned} P(c|\nu ABCD\sigma\lambda_{\mathrm{SO}}^g\lambda_{\mathrm{SO}}^e c^{e/g}S_TS_A\beta I) &= \sum_{n=0}^{c} e^{-c_e}\frac{{c_e}^n}{n!}e^{-\beta}\frac{\beta^{(c-n)}}{(c-n)!} \\ &= e^{-(c_e+\beta)}\sum_{n=0}^{c}\frac{{c_e}^n}{n!}\frac{\beta^{(c-n)}}{(c-n)!} \\ &= \frac{e^{-(c_e+\beta)}}{c!}\sum_{n=0}^{c}\binom{c}{n}{c_e}^n\beta^{(c-n)} \\ &= \frac{e^{-(c_e+\beta)}}{c!}(c_e+\beta)^c. \end{aligned} \tag{C2}$$

The problematic sum has been handled with use of the binomial-sum relation. Again, to avoid overflow errors for large c, we consider the log probability:

$$\log\left(P(c|\nu ABCD\sigma\lambda_{\mathrm{SO}}^g\lambda_{\mathrm{SO}}^e c^{e/g}S_TS_A\beta I)\right) = -(c_e+\beta) - \log(c!) + c\log(c_e+\beta). \tag{C3}$$

This probability is formally called the "likelihood."

2. Bayesian inference

With this encoding of the model into an expression for the likelihood of observed count values at each pixel of each spectrum, we can apply Bayes's rule to obtain

$$\begin{aligned} P(ABCD\sigma\lambda_{\mathrm{SO}}^g\lambda_{\mathrm{SO}}^e c^{e/g}S_TS_A\beta|\vec{c}I) &= \sum P(c|\nu ABCD\sigma\lambda_{\mathrm{SO}}^g\lambda_{\mathrm{SO}}^e c^{e/g}S_TS_A\beta I) \\ &\quad\times P(\nu ABCD\sigma\lambda_{\mathrm{SO}}^g\lambda_{\mathrm{SO}}^e c^{e/g}S_TS_A|\beta I) \\ &\quad/P(c|I), \end{aligned} \tag{C4}$$

where the sum is across all pixels of all the spectra under consideration and all but the parameters λ_{SO}^g, λ_{SO}^e, and $c^{e/g}$ are different between each spectrum.

This is an elaborate computation because for the 17 spectra examined here, there are 139 free parameters to be inferred. The prior [Eq. (C4)] for this inference consisted of various constraints, comprising

(a) All linewidths σ must be positive.
(b) All transverse strains S_T must be positive.
(c) The ground-state spin-orbit splitting λ_{SO}^g must be less than 50 GHz (on the basis of published data for Si-V^- with observed ground-state splittings less than 50 GHz).
(d) All peak amplitudes A, B, C, D must remain above 60% of their initial guesses (manually obtained by visual approximation).

The probability given in Eq. (C3) is obtained with a MCMC-ensemble-sampler algorithm. Many of the model

parameters (such as peak amplitude) are not important for the discussion of transverse strain, and it is possible to integrate them out by invoking the fact that the integral across all space of any probability must have a value of 1. In this way it is possible to obtain the probability $P(\lambda_{SO}^{g}\lambda_{SO}^{e}c^{e/g}|\vec{c}I)$, which represents knowledge of fundamental Si-V^- parameters on the basis of all the PL spectra that are considered. The MCMC-sampler chain trajectories and final probability distributions for these three Hamiltonian parameters are shown in Fig. 8.

It is important to point out that the probability distributions are not Gaussian, and that especially λ_{SO}^{g} is not even symmetric. For the ground-state spin-orbit splitting the asymmetry is clearly connected to the prior, which constrains this value to remain below 50 GHz. A similar shape is observed in Fig. 8(d) for the excited-state spin-orbit splitting. This occurs even though no constraint is imposed on λ_{SO}^{e}, and demonstrates the tight relationship established between these parameters on the basis of the spectral data. Indeed, this is confirmed by the narrow distribution of the splitting coefficient ratio in Fig. 8(f). The non-Gaussian nature of these distributions means that the uncertainties (which are given as 95% credible regions) may in places overstate the breadth of the probability distribution if they are interpreted as relating to standard deviations.

3. Discussion

Beyond the three fundamental Si-V^- parameters represented in Fig. 8, each PL spectrum has eight additional parameters required to describe it according to the model presented here. It is possible to examine the MCMC-sampler trajectories for all of these parameters, and the spectrum for spot 1 is shown in Fig. 9 as a representative example. For each spectrum, suitable "approximate values" are obtained for these parameters in a manual visual process. The MCMC-sampler seed values are randomly generated in a range of a few percent around these visual estimates. It is clear that some parameters reach their equilibrium distributions quickly, and these tend to be those that are not "coupled" to any others (such as the background count).

Considering the peaks A, B, C and D of the corresponding optical transitions referred in Fig. 1, careful examination of Fig. 10 reveals that spots 8 and 18 appear to be misplaced on the transverse-strain axis, toward lower

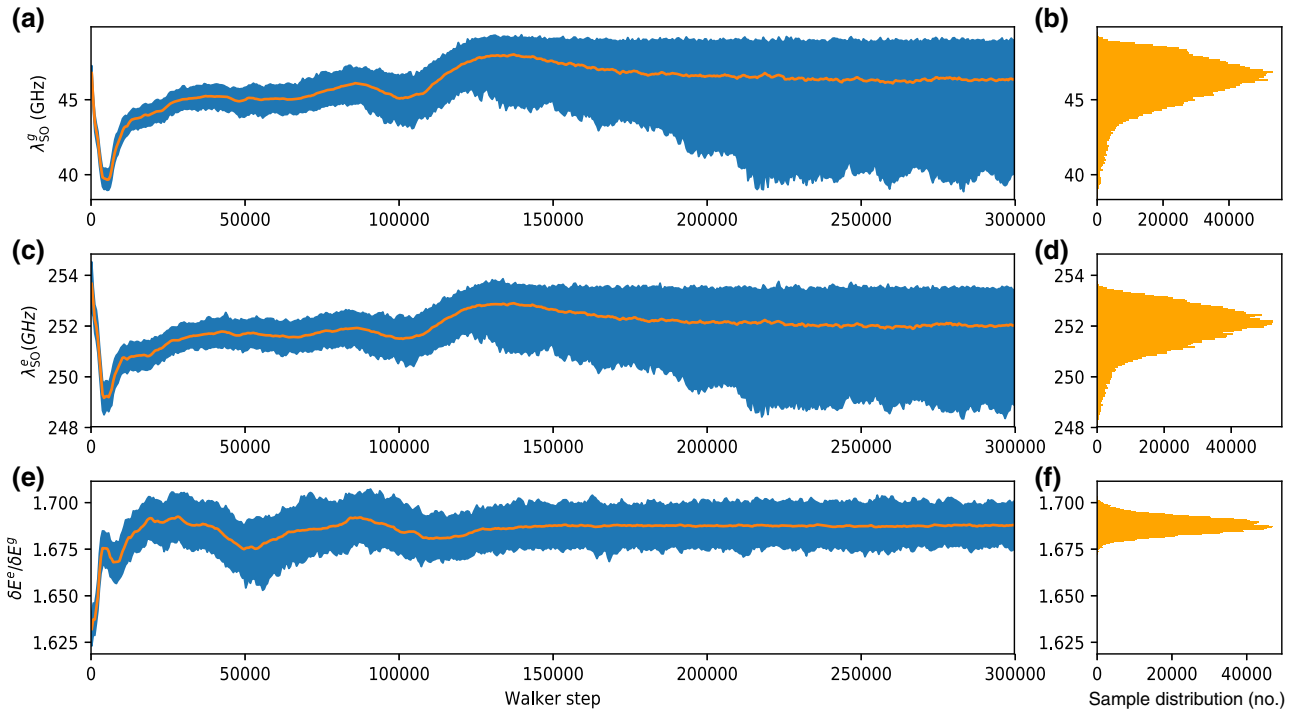

FIG. 8. MCMC-sampler chain trajectories for the fundamental Si-V^- Hamiltonian parameters. (a) Median (orange line) and 95% credible region (blue shading) of the distribution of MCMC walkers for the ground-state spin-orbit splitting λ_{SO}^{g}. The credible region and median are calculated for blocks of 50 steps at a time. Initial guesses are distributed randomly in the neighborhood of 47 GHz. On the basis of previously reported Si-V^- ground-state splittings less than 50 GHz, this parameter is constrained by a prior limiting it to values less than 50 GHz. It is apparent that from about 125 000 steps the distribution is skewed by this constraint. (b) Histogram showing the final distribution of the MCMC samples, calculated for the final 5000 steps. (c),(d) Walker trajectory and final distribution of samples for the excited-state spin-orbit splitting λ_{SO}^{e}. (e),(f) Walker trajectory and final distribution of samples for the ratio of transverse-strain coefficients $\delta E^e/\delta E^g$.

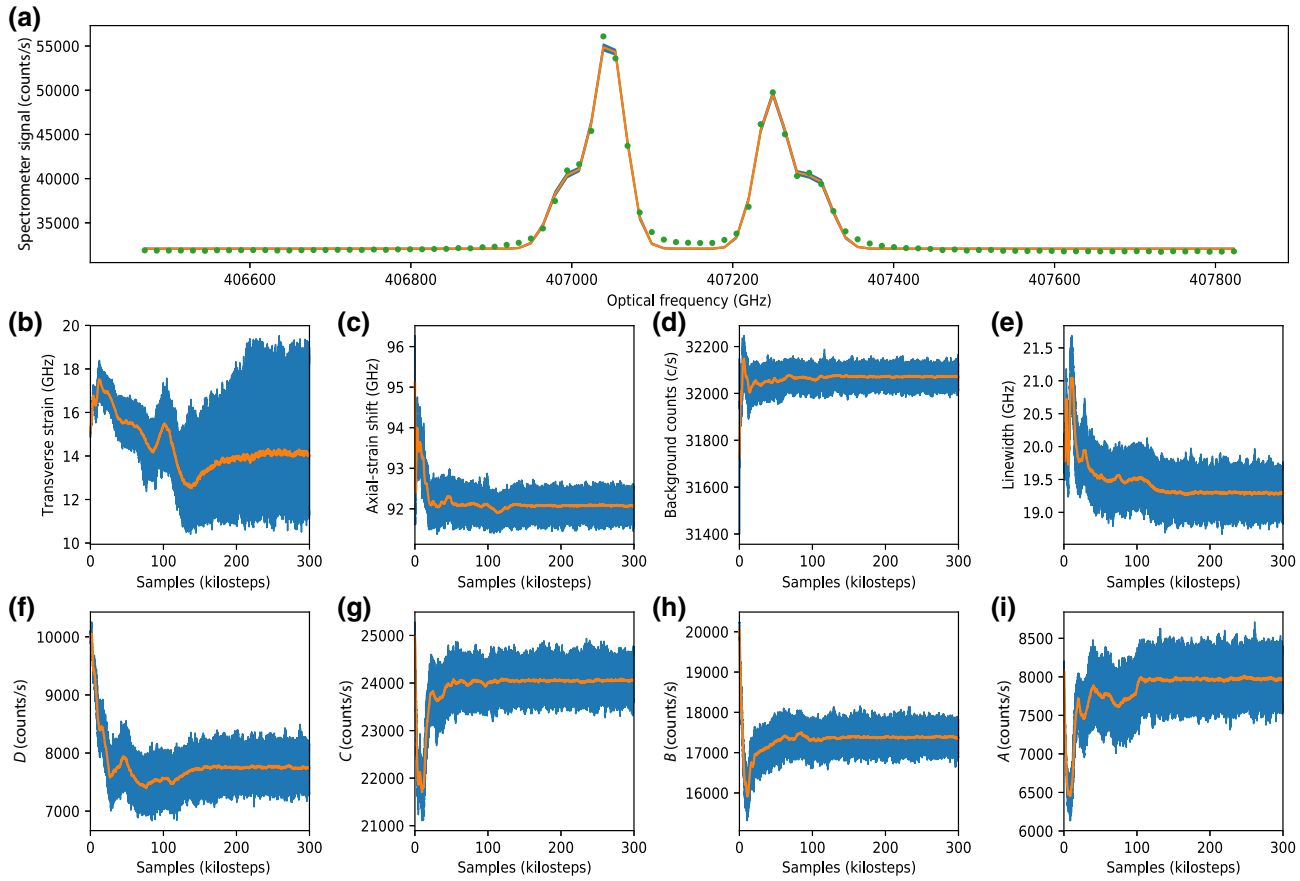

FIG. 9. Spectrum and MCMC-sampler chain trajectories for parameters specific to Si-V^- spot 1. (a) The Bayesian analysis infers Hamiltonian parameters directly from the raw spectral data (green circles). The final "fit" is represented by the median (orange line) and 95% credible region (blue shading). (b) The MCMC-sampler chain trajectory for the transverse strain of this spot. This parameter provides the horizontal positioning of the spectrum in the strain-summary figure [Figs. 8 and 3(e)]. (c) Sampler trajectory for the axial-strain term for this spot. This affects the shift of the ZPL and therefore considers all four peaks together, and so it is not surprising that this parameter reaches equilibrium in the sampler trajectory more quickly than the transverse strain. (d) Sampler trajectory for the background count. There are a lot of CCD pixels that measure almost nothing but background, and so it is unsurprising that this parameter quickly reaches equilibrium in the sampler trajectory. (e) Sampler trajectory for the linewidth. Since the linewidth is limited by the instrument or by temperature, our model takes the same width for all four peaks in the spectrum. (f)–(i) Sampler trajectories for the amplitudes D, C, B, and A of the four peaks. Peak position matters for the strain analysis, but peak height is not important. Here it is visually apparent that sensible values are obtained.

strain than the outer peaks A and D would indicate. While it is normal for fitted data not to be represented exactly by a fit, the prior in Bayesian inference favors here the significance of lines B and C and therefore seems to increase the error for A and D. This occurs because the outer peaks A and D are much weaker in these spectra than the inner peaks B and C. As a result, the MCMC sampler has prioritized matching the splitting of inner peaks at the expense of the outer peaks. To do this the MCMC sampler has reduced its "fit" inference for the amplitudes A and D, and has in fact "hit against" the minimum-peak-height constraint of the prior. In this case, it is mathematically more likely that the small, outer peaks arise due to noise than that the inner peaks are slightly offset from their "true" position. Any more-extreme mistreatment of the outer peaks A and D is prevented by the prior constraints that are imposed for the amplitudes of these peaks (they are required to stay above 60% of the manually identified initial guesses).

The expanded view in Fig. 10 shows that spot 5 has a linewidth considerably greater than for most of the other spots, and the ground-state splitting is not resolved in the spectrum. This is interpreted to be the result of elevated temperature, probably occurring due to poor thermal contact between the ND and the cold finger of the cryostat. The inability to resolve the ground-state splitting means that this spectrum is not included in Figs. 3(c) and 3(d).

Since the spectra are fit with the strain model for the Si-V^- spectrum, spurious peaks in the measurements have little impact. Spots 11 and 13 clearly have an extra peak, but the model requires symmetric splittings in the spectrum,

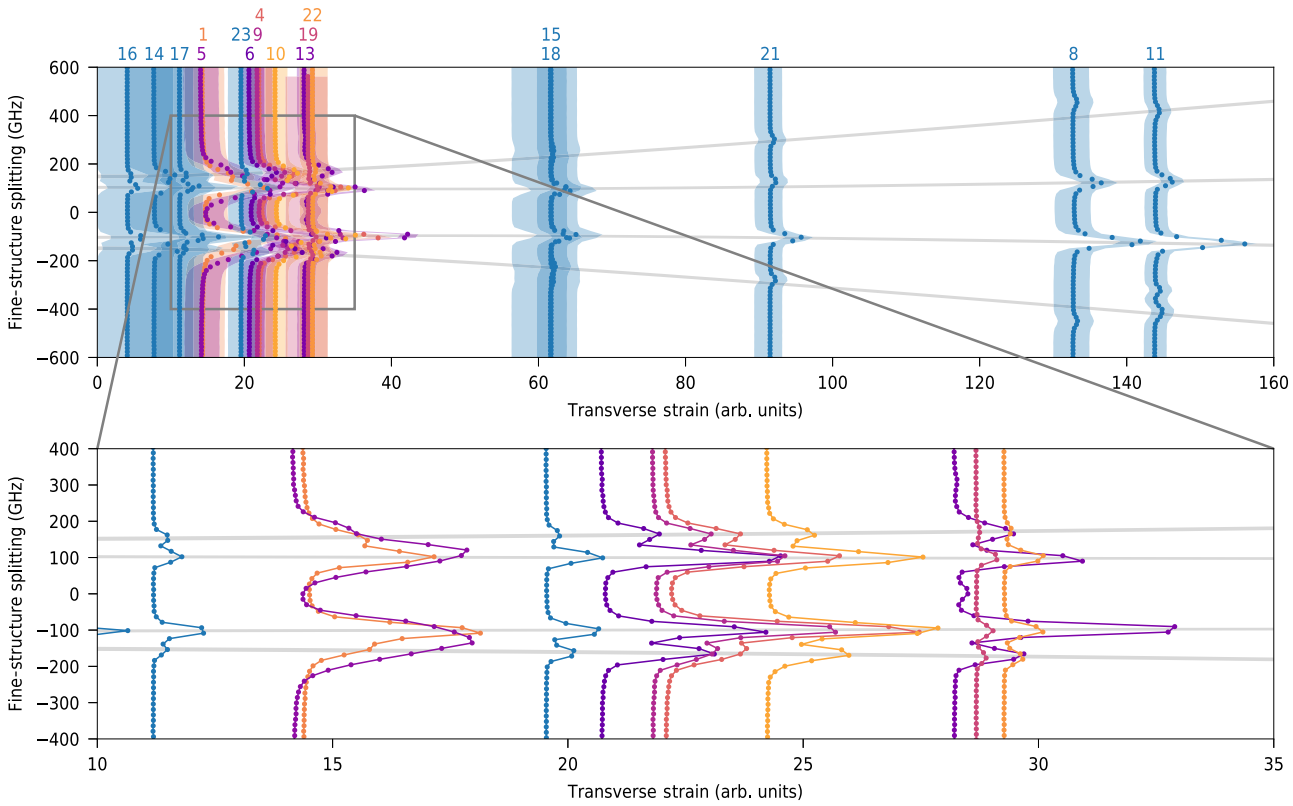

FIG. 10. Strain analysis with expanded detail. This is a reproduction of Fig. 3(e), with the spectra annotated by their "focal spot number." Not all of the recorded spectra have a clear-enough "single Si-V^-" structure to be used in this analysis. The inset shows more detail of the dense region at low strain, which contains numerous almost-overlapping spectra. The 95%-credible-region shading has been omitted from the inset for better viewing of the individual spectra.

and so any attempted fit to the "wrong" peak was automatically suppressed. This extra peak would have marginally offset the background counts but not effected any other parameter.

In the strain model, the transition energies remain fairly constant for low strain. This is due to the splittings being dominated by spin-orbit interaction. As a result, it is difficult to precisely determine the strain value for a spectrum with minimal strain splitting. For this reason, the 95% credible region for transverse strain is expanded for spots 16, 14, and 17. For spots 16 and 14 the MCMC-sampler distributions for transverse strain "hit against" the constraint that required positive transverse-strain splitting. All in all this does not mean that the strain model misrepresents many points. The Bayesian-inference algorithm does not fit single spectra but fits the whole set of data to a model and determines the values for that fit for the dataset as a whole. Therefore, there are no individual fits for an individual spectrum. Every line fit is merely a projection of the model onto the transverse-strain value.

[1] Serge Haroche, Controlling photons in a box and exploring the quantum to classical boundary: Controlling photons in a box and exploring the quantum to classical boundary, Ann. Phys. **525**, 753 (2013).

[2] David J. Wineland, Nobel Lecture: Superposition, entanglement, and raising Schrödinger's cat, Rev. Mod. Phys. **85**, 1103 (2013).

[3] C. Monroe and J. Kim, Scaling the ion trap quantum processor, Science **339**, 1164 (2013).

[4] M. H. Devoret and R. J. Schoelkopf, Superconducting circuits for quantum information: An outlook, Science **339**, 1169 (2013).

[5] Manuel Endres, Hannes Bernien, Alexander Keesling, Harry Levine, Eric R. Anschuetz, Alexandre Krajenbrink, Crystal Senko, Vladan Vuletic, Markus Greiner, and Mikhail D. Lukin, Atom-by-atom assembly of defect-free one-dimensional cold atom arrays, Science **354**, 1024 (2016).

[6] Jeremy L. O'Brien, Akira Furusawa, and Jelena Vučković, Photonic quantum technologies, Nat. Photonics **3**, 687 (2009).

[7] H. J. Kimble, The quantum internet, Nature **453**, 1023 (2008).

[8] Stephan Ritter, Christian Nölleke, Carolin Hahn, Andreas Reiserer, Andreas Neuzner, Manuel Uphoff, Martin Mücke, Eden Figueroa, Joerg Bochmann, and Gerhard Rempe, An elementary quantum network of single atoms in optical cavities, Nature **484**, 195 (2012).

[9] Tim Schröder, Matthew E. Trusheim, Michael Walsh, Luozhou Li, Jiabao Zheng, Marco Schukraft, Alp Sipahigil, Ruffin E. Evans, Denis D. Sukachev, Christian T. Nguyen, Jose L. Pacheco, Ryan M. Camacho, Edward S. Bielejec, Mikhail D. Lukin, and Dirk Englund, Scalable focused ion beam creation of nearly lifetime-limited single quantum emitters in diamond nanostructures, Nat. Commun. **8**, 15376 (2017).

[10] A. Sipahigil, R. E. Evans, D. D. Sukachev, M. J. Burek, J. Borregaard, M. K. Bhaskar, C. T. Nguyen, J. L. Pacheco, H. A. Atikian, C. Meuwly, R. M. Camacho, F. Jelezko, E. Bielejec, H. Park, M. Lončar, and M. D. Lukin, An integrated diamond nanophotonics platform for quantum-optical networks, Science **354**, 847 (2016).

[11] L. J. Rogers, K. D. Jahnke, T. Teraji, L. Marseglia, C. Müller, B. Naydenov, H. Schauffert, C. Kranz, J. Isoya, L. P. McGuinness, and F. Jelezko, Multiple intrinsically identical single-photon emitters in the solid state, Nat. Commun. **5**, 4739 (2014).

[12] A. Sipahigil, K. D. Jahnke, L. J. Rogers, T. Teraji, J. Isoya, A. S. Zibrov, F. Jelezko, and M. D. Lukin, Indistinguishable Photons from Separated Silicon-Vacancy Centers in Diamond, Phys. Rev. Lett. **113**, 113602 (2014).

[13] Christian Hepp, Tina Müller, Victor Waselowski, Jonas N. Becker, Benjamin Pingault, Hadwig Sternschulte, Doris Steinmüller-Nethl, Adam Gali, Jeronimo R. Maze, Mete Atatüre, and Christoph Becher, Electronic Structure of the Silicon Vacancy Color Center in Diamond, Phys. Rev. Lett. **112**, 036405 (2014).

[14] Alan T. Collins, Lars Allers, Christopher J. H. Wort, and Geoffrey A. Scarsbrook, The annealing of radiation damage in De Beers colourless CVD diamond, Diam. Relat. Mater. **3**, 932 (1994).

[15] Syuto Tamura, Godai Koike, Akira Komatsubara, Tokuyuki Teraji, Shinobu Onoda, Liam P. McGuinness, Lachlan Rogers, Boris Naydenov, E. Wu, Liu Yan, Fedor Jelezko, Takeshi Ohshima, Junichi Isoya, Takahiro Shinada, and Takashi Tanii, Array of bright silicon-vacancy centers in diamond fabricated by low-energy focused ion beam implantation, Appl. Phys. Express **7**, 115201 (2014).

[16] Janik Wolters, Günter Kewes, Andreas W. Schell, Nils Nüsse, Max Schoengen, Bernd Löchel, Tobias Hanke, Rudolf Bratschitsch, Alfred Leitenstorfer, Thomas Aichele, and Oliver Benson, Coupling of single nitrogen-vacancy defect centers in diamond nanocrystals to optical antennas and photonic crystal cavities, Phys. Status Solidi (B) **249**, 918 (2012).

[17] Mikhail Y. Shalaginov, Vadim V. Vorobyov, Jing Liu, Marcello Ferrera, Alexey V. Akimov, Alexei Lagutchev, Andrey N. Smolyaninov, Vasily V. Klimov, Joseph Irudayaraj, Alexander V. Kildishev, Alexandra Boltasseva, and Vladimir M. Shalaev, Enhancement of single-photon emission from nitrogen-vacancy centers with TiN/(Al,Sc)N hyperbolic metamaterial: Enhancement of single-photon emission, Laser Photon. Rev. **9**, 120 (2015).

[18] Alexander Huck and Ulrik L. Andersen, Coupling single emitters to quantum plasmonic circuits, Nanophotonics **5**, 483 (2016).

[19] Uwe Jantzen, Andrea B. Kurz, Daniel S. Rudnicki, Clemens Schäfermeier, Kay D. Jahnke, Ulrik L. Andersen, Valery A Davydov, Viatcheslav N. Agafonov, Alexander Kubanek, Lachlan J. Rogers, and Fedor Jelezko, Nanodiamonds carrying silicon-vacancy quantum emitters with almost lifetime-limited linewidths, New J. Phys. **18**, 073036 (2016).

[20] Alexander Huck, Shailesh Kumar, Abdul Shakoor, and Ulrik L. Andersen, Controlled Coupling of a Single Nitrogen-Vacancy Center to a Silver Nanowire, Phys. Rev. Lett. **106**, 096801 (2011).

[21] V. A. Davydov, A. V. Rakhmanina, S. G. Lyapin, I. D. Ilichev, K. N. Boldyrev, A. A. Shiryaev, and V. N. Agafonov, Production of nano- and microdiamonds with Si-V and N-V luminescent centers at high pressures in systems based on mixtures of hydrocarbon and fluorocarbon compounds, JETP. Lett. **99**, 585 (2014).

[22] Jan M. Binder, Alexander Stark, Nikolas Tomek, Jochen Scheuer, Florian Frank, Kay D. Jahnke, Christoph Müller, Simon Schmitt, Mathias H. Metsch, Thomas Unden, Tobias Gehring, Alexander Huck, Ulrik L. Andersen, Lachlan J. Rogers, and Fedor Jelezko, Qudi: A modular python suite for experiment control and data processing, Software X **6**, 85 (2017).

[23] Daniel Foreman-Mackey, David W. Hogg, Dustin Lang, and Jonathan Goodman, emcee: The MCMC hammer, Publ. Astron. Soc. Pac. **125**, 306 (2013).

[24] Anand Patil, David Huard, and Christopher J. Fonnesbeck, PyMC: Bayesian stochastic modelling in python, J. Stat. Softw. **35**, 1 (2010).

[25] Eric O. Lebigot, Uncertainties: A Python package for calculations with uncertainties.

[26] E. Neu, C. Arend, E. Gross, F. Guldner, C. Hepp, D. Steinmetz, E. Zscherpel, S. Ghodbane, H. Sternschulte, D. Steinmüller-Nethl, Y. Liang, A. Krueger, and C. Becher, Narrowband fluorescent nanodiamonds produced from chemical vapor deposition films, Appl. Phys. Lett. **98**, 243107 (2011).

[27] Lachlan J. Rogers, Kay D. Jahnke, Marcus W. Doherty, Andreas Dietrich, Liam P. McGuinness, Christoph Müller, Tokuyuki Teraji, Hitoshi Sumiya, Junichi Isoya, Neil B. Manson, and Fedor Jelezko, Electronic structure of the negatively charged silicon-vacancy center in diamond, Phys. Rev. B **89**, 235101 (2014).

[28] Kay D. Jahnke, Alp Sipahigil, Jan M. Binder, Marcus W. Doherty, Mathias Metsch, Lachlan J. Rogers, Neil B. Manson, Mikhail D. Lukin, and Fedor Jelezko, Electron-phonon processes of the silicon-vacancy centre in diamond, New J. Phys. **17**, 043011 (2015).

[29] Andreas Dietrich, Kay D. Jahnke, Jan M. Binder, Tokuyuki Teraji, Junichi Isoya, Lachlan J. Rogers, and Fedor Jelezko, Isotopically varying spectral features of silicon-vacancy in diamond, New J. Phys. **16**, 113019 (2014).

[30] H. Sternschulte, K. Thonke, R. Sauer, P. C. Münzinger, and P. Michler, 1.681-eV luminescence center in chemical-vapor-deposited homoepitaxial diamond films, Phys. Rev. B **50**, 14554 (1994).

[31] E. T. Jaynes, *Probability Theory: the Logic of Science* (Cambridge University Press, 2003).

[32] Phil Gregory, *Bayesian Logical Data Analysis for the Physical Sciences: A Comparative Approach with Mathematica® Support* (Cambridge University Press, 2005).

[33] Gopalakrishnan Balasubramanian, I. Y. Chan, Roman Kolesov, Mohannad Al-Hmoud, Julia Tisler, Chang Shin, Changdong Kim, Aleksander Wojcik, Philip R. Hemmer, Anke Krueger, Tobias Hanke, Alfred Leitenstorfer, Rudolf Bratschitsch, Fedor Jelezko, and Jörg Wrachtrup, Nanoscale imaging magnetometry with diamond spins under ambient conditions, Nature **455**, 648 (2008).

[34] Victor Marcel Acosta, *Optical magnetometry with nitrogen-vacancy centers in diamond* (University of California, Berkeley, 2011).

[35] M. V. Hauf, B. Grotz, B. Naydenov, M. Dankerl, S. Pezzagna, J. Meijer, F. Jelezko, J. Wrachtrup, M. Stutzmann, F. Reinhard, and J. A. Garrido, Chemical control of the charge state of nitrogen-vacancy centers in diamond, Phys. Rev. B **83**, 081304 (2011).

[36] Ruffin E. Evans, Alp Sipahigil, Denis D. Sukachev, Alexander S. Zibrov, and Mikhail D. Lukin, Narrow-Linewidth Homogeneous Optical Emitters in Diamond Nanostructures via Silicon Ion Implantation, Phys. Rev. Appl. **5**, 044010 (2016).

[37] J. Meijer, B. Burchard, M. Domhan, C. Wittmann, T. Gaebel, I. Popa, F. Jelezko, and J. Wrachtrup, Generation of single color centers by focused nitrogen implantation, Appl. Phys. Lett. **87**, 261909 (2005).

[38] J. R. Rabeau, P. Reichart, G. Tamanyan, D. N. Jamieson, S. Prawer, F. Jelezko, T. Gaebel, I. Popa, M. Domhan, and J. Wrachtrup, Implantation of labelled single nitrogen vacancy centers in diamond using N15, Appl. Phys. Lett. **88**, 023113 (2006).

[39] Thomas A. Klar and Stefan W. Hell, Subdiffraction resolution in far-field fluorescence microscopy, Opt. Lett. **24**, 954 (1999).

[40] Lachlan J. Rogers, Kay D. Jahnke, Mathias H. Metsch, Alp Sipahigil, Jan M. Binder, Tokuyuki Teraji, Hitoshi Sumiya, Junichi Isoya, Mikhail D. Lukin, Philip Hemmer, and Fedor Jelezko, All-optical initialization, readout, and coherent preparation of single silicon-vacancy spins in diamond, Phys. Rev. Lett. **113**, 263602 (2014).

[41] Benjamin Pingault, Jonas N. Becker, Carsten H. H. Schulte, Carsten Arend, Christian Hepp, Tillmann Godde, Alexander I. Tartakovskii, Matthew Markham, Christoph Becher, and Mete Atatüre, All-Optical Formation of Coherent Dark States of Silicon-Vacancy Spins in Diamond, Phys. Rev. Lett. **113**, 263601 (2014).

[42] Jonas Nils Becker, Johannes Görlitz, Carsten Arend, Matthew Markham, and Christoph Becher, Ultrafast all-optical coherent control of single silicon vacancy colour centres in diamond, Nat. Commun. **7**, 13512 (2016).

[43] Benjamin Pingault, David-Dominik Jarausch, Christian Hepp, Lina Klintberg, Jonas N. Becker, Matthew Markham, Christoph Becher, and Mete Atatüre, Coherent control of the silicon-vacancy spin in diamond, Nat. Commun. **8**, 15579 (2017).

[44] D. D. Sukachev, A. Sipahigil, C. T. Nguyen, M. K. Bhaskar, R. E. Evans, F. Jelezko, and M. D. Lukin, Silicon-Vacancy Spin Qubit in Diamond: A Quantum Memory Exceeding 10 ms with Single-Shot State Readout, Phys. Rev. Lett. **119**, 223602 (2017).

[45] Srujan Meesala, Young-Ik Sohn, Benjamin Pingault, Linbo Shao, Haig A. Atikian, Jeffrey Holzgrafe, Mustafa Gündoğan, Camille Stavrakas, Alp Sipahigil, Cleaven Chia, Ruffin Evans, Michael J. Burek, Mian Zhang, Lue Wu, Jose L. Pacheco, John Abraham, Edward Bielejec, Mikhail D. Lukin, Mete Atatüre, and Marko Lončar, Strain engineering of the silicon-vacancy center in diamond, Phys. Rev. B **97**, 205444 (2018).

[46] Rosa Brouri, Alexios Beveratos, Jean-Philippe Poizat, and Philippe Grangier, Photon antibunching in the fluorescence of individual color centers in diamond, Opt. Lett. **25**, 1294 (2000).